A CONTROL SYSTEMS PERSPECTIVE ON NANOINTERROGATION

Scanning Probe Microscopy

SRINIVASA M. SALAPAKA
and MURTI V. SALAPAKA

At the 1959 annual meeting of the American Physical Society, Richard Feynman gave a seminal talk titled "There's Plenty of Room at the Bottom." In this talk [1], Feynman presented a vision that embodies the accomplishments and promise of nanotechnology and nanoscience. He asserted that laws of physics do not prevent manipulation and interrogation of material at the atomic scale. For achieving such a capability, he discussed concepts for improving electron microscopes and conceived a hierarchy of mechanical devices, where successive layers yield increasing resolution. He also provided a tantalizing glimpse of the potential impact of the ability to manipulate and interrogate matter at the atomic scale. He postulated that such an ability can lead to technologies such as high-density data storage, materials designed with specificity at the atomic scale, and miniature computing devices.

The invention of the scanning tunneling microscope (STM) is a significant step in realizing the vision of atomic-scale interrogation of materials. The STM uses the quantum-mechanical phenomenon of *tunneling current*. Tunneling current is caused by the flow of electrons from the surface of one material to the surface of another even when the surfaces are not in contact with each other. The magnitude of the tunneling current is appreciable when the separation between the surfaces is on the order of a few nanometers. In scanning tunneling microscopy, the tunneling current flows between the *sample*, which is the material being imaged, and the *probe*, which is positioned above the sample. The STM determines the topography of the material by using the dependence of the tunneling current on the separation between the two surfaces. Earlier attempts to use tunneling current to image material with atomic-scale resolution were not successful due to extraneous vibrations that made it difficult to maintain a small separation between the probe and the sample.

In 1981, Binnig and Rohrer conducted the first successful tunneling experiment [2]. A feedback loop that controlled the gap between the surfaces of the probe and the

IMAGE: JOSEPH STROSCIO; ROBERT CELOTTA/NIST

Digital Object Identifier 10.1109/MCS.2007.914688

1066-033X/08/$25.00©2008IEEE

Power of Scanning Probe Microscopes

The invention of the STM and AFM are landmark events in the history of nanoscience and nanotechnology. Prior to the invention of the STM and AFM, interrogating the structure of material with atomic-scale precision was cumbersome, expensive, and difficult. Since the invention of these instruments, atomic-scale interrogation of matter has become simple and inexpensive.

The invention of the STM and AFM have heralded a new family of instruments: SPMs. SPMs share the operating principles of the STM and AFM, which are based on the use of a probe and the ability to position the material of interest in relation to the probe with atomic-scale precision. Various members of the SPM family differ in the nature of the probes that are employed, which are chosen based on the specific property of the material being interrogated. STMs employ a sharp conducting tip as the probe, whereas AFMs use a microfabricated cantilever with a sharp tip as a force transducer. Magnetic, thermal, and biological properties of material can be interrogated at the atomic scale by suitably altering or changing the probe. For example, a magnetic force microscope, a member of the SPM family, images magnetic forces by coating the tip of an AFM cantilever with a magnetic material such as cobalt. Similarly, by suitably modifying the tip with biological material, the AFM probe can be made sensitive to biomolecular forces.

In addition to interrogation at the nanoscale, the SPM can be used to alter material at the nanoscale. The cantilever probe in the AFM can be used as a nanolithography tool, where sufficient force can be applied by the tip of the cantilever to etch the material. Similarly, the cantilever tip can be used to deposit biological material on a surface, whereas a magnetized tip can change the orientation of the magnetic domains of the material. Thus, SPM provides a versatile method for probing as well as manipulating material at the nanoscale.

SPMs with the ability to interrogate, control, and manipulate various properties of matter at the atomic scale, together with the ability to operate in different environments, are having a dramatic impact on fields as diverse as biology, materials science, electrochemistry, tribology, biochemistry, surface physics, and medicine (Figure S1). Apart from their impact on science, SPMs are leading to new technologies. For example, the ability to manipulate and sense the topography of material at the nanoscale has resulted in new technologies for high-density data storage [49]. Similarly, the ability to modify material biologically is leading to biomolecular assays that can be used for drug discovery [50].

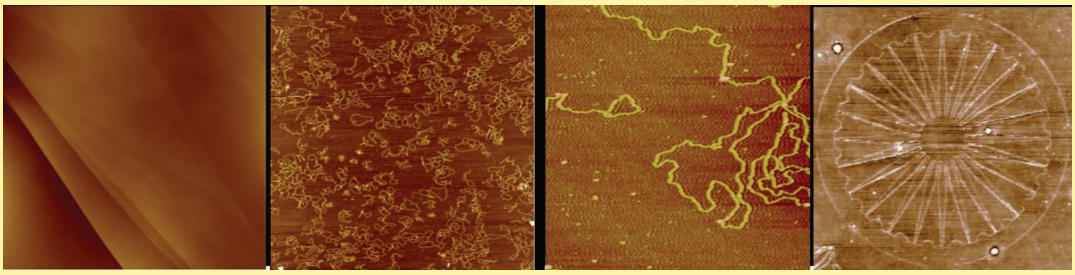

FIGURE S1 Manipulation, investigation, and control in the nano world. (a) Graphite with multiple layers; the layers are separated by distances that are integer multiples of 3.4 Å. (b) Plasmid deoxyribonucleic acid (DNA) with a scan size of 4 μm by 4 μm; the loop structure of the DNA molecule is evident, and the DNA height is approximately 1.2 nm. (c) A zoomed image of a plasmid DNA. (d) An intricate pattern is etched onto a polycarbonate surface using the cantilever tip. The image size is 4 μm by 4 μm.

sample was pivotal to the success of their experiment. Binnig and Rohrer also realized that their setup could be used to image the topography of material at the atomic scale [3], and their team subsequently used the STM to resolve the structure of silicon at the atomic scale [4]. Earlier work on imaging with atomic-scale resolution was achieved with either field-ion microscopy or electron microscopy. In contrast to field-ion and electron microscopes, the attractive feature of the STM is that it makes interrogation of matter with atomic-scale resolution simple and affordable. For details on the impact of these devices, see "Power of Scanning Probe Microscopes." Binnig and Rohrer were awarded the Nobel prize in physics for the STM in 1986.

The use of STM is limited to conductors and semiconductors. Imaging with atomic-scale resolution for insulators was unavailable until 1986, when Binnig, Quate, and Gerber invented the atomic force microscope (AFM). This device heralded a new class of instruments, *scanning probe microscopes* (SPMs), which are based on variants of STM and AFM principles. The 2000 U.S. National Nanotechnology Initiative noted that "STMs, AFMs, and near-field microscopes provide the eyes and fingers required for nanostructure, manipulation, and measurement" [5].

The inventors of the AFM and the STM were aware of the role of feedback strategies, and they used proportional-integral (PI) controllers to great effect. Earlier research related to scanning probe microscopy focused on the underlying physical processes affecting the instruments. The demands imposed by users of SPM technology include faster imaging, higher resolution imaging, robust operation, and quantitative measures of image fidelity. Although classical and simple control strategies were used in early STMs and AFMs, modern control and systems tools are needed to meet the demands of future SPM technology.

This article presents the role of system-theoretic tools in providing new insights into phenomena observed in current nanoscience studies and in expanding existing technology related to interrogation of material at the nanoscale.

BASIC OPERATING PRINCIPLES

Scanning Tunneling Microscopy

The tunneling current I_T in terms of the separation z between two surfaces is given by

$$I_T(z) = I_0(V)e^{-2\kappa z}, \tag{1}$$

where the parameters κ and $I_0(V)$ are material-dependent constants [6] and V is the voltage difference across the two surfaces. For a typical conducting material, κ is on the order of 10^{10} m^{-1}. The large exponent κ implies that the contribution to the tunneling current decreases by a factor of ten for an atom that is two atomic dimensions farther from the tip. Since most of the contribution to the tunneling current is due to the atom on the sample surface that is closest to the tip, STM can determine the sample topography with atomic resolution.

Since a sample is typically tilted, it is difficult to move the sample laterally without either losing proximity between the tip and the sample or impacting the tip into the sample. Another practical difficulty in using the tunneling current to image the topography of the sample is the nonlinear dependence of the tunneling current on the sample height. Only the qualitative behavior of the relation (1) is known, which limits the ability to determine the topography of the sample from the tunneling current.

Scanning tunneling microscopy uses feedback to overcome the practical difficulties that limit the use of tunneling current. In STMs, a feedback scheme is used to vertically position the sample with respect to the tip with the objective of maintaining a constant current (Figure 1). During a *scan*, when the sample is moved laterally under the tip, the controller attempts to maintain a constant current by moving the sample vertically in a manner that compensates for variations in the topography of the sample. Thus, during scanning, when the separation between the sample and the tip decreases or increases due to variations in the sample topography, the control signal regulates the current by actuating the positioning device away from or toward the tip. For typical speeds of operation, the compensating control signal is proportional to variations in the topography and therefore provides a measure of the sample topography. This feedback scheme restricts the movement of the tip to a small region around an operating point of the current-separation curve described by (1), and, therefore, linear behavior of the current with respect to separation z can be assumed. The linearizing effect is a significant advantage of the control loop.

The STM feedback mechanism requires a positioning device that provides subangstrom resolution at an acceptable bandwidth. Piezoelectric elements provide such a high positioning resolution. A contribution of early STM experiments is confirmation that piezoelectric material can be deformed with the required resolution.

Atomic Force Microscopy

Atomic force microscopy relies on the ability to sense small forces. A cantilever with a sharp tip provides the means for sensing forces exerted on the tip by the atoms in the sample. To register small interatomic forces, the cantilever probe must be insensitive to extraneous disturbances from the surrounding environment. These disturbances are caused by sources such as building vibrations, whose power spectral density is significant in the frequency range 0–2 kHz. Therefore, to avoid the effects of these disturbances, the resonance frequency of the cantilever must be greater than 2 kHz. At the same time, the cantilevers need to be sufficiently compliant to sense the interatomic forces.

The forces between the tip of the cantilever and the sample are in the range 10^{-7}–10^{-12} N. To produce a

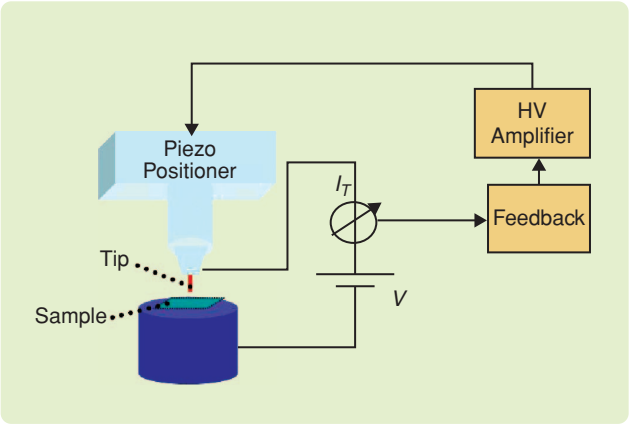

FIGURE 1 Scanning tunneling microscope. The scanning tunneling microscope yields atomic resolution by exploiting the tunneling current I_T between a sharp tip and the sample. The tunneling current depends on the tip-sample separation. The force-balance principle is employed where the control signal forms the image.

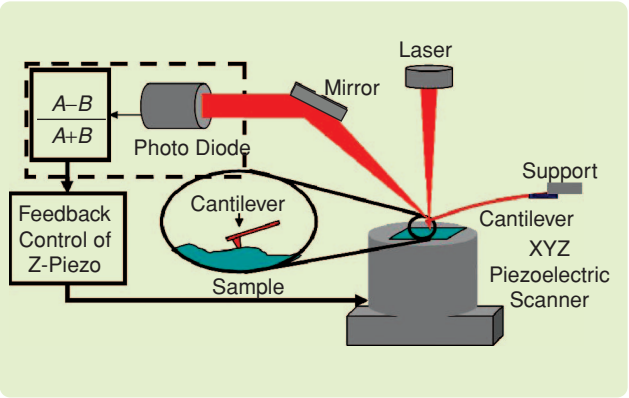

FIGURE 2 Atomic force microscope. Unlike the scanning tunneling microscope, the atomic force microscope yields atomic-resolution imaging capability for both conductors and insulators. The main probe of an atomic force microscope is a microcantilever, which deflects due to forces between the atoms on the sample and the atoms on the tip. The deflection of the cantilever is registered by a laser incident on the cantilever, which reflects onto a split photodiode. The cantilever support can be forced using the dither piezo. The control signal, which regulates a reference setpoint by moving the sample vertically relative to the cantilever probe, gives a measure of the sample topography. A piezo scanner positions the sample relative to the cantilever in the lateral and the vertical directions.

deflection greater than 1 Å for a force of 10^{-12} N, the spring constant k of the cantilever must be less than 0.01 N/m. A stiffness of 0.01 N/m and a resonance frequency of 2 kHz implies a mass less than 10^{-10} kg. These requirements are met by microcantilevers, which are typically made of silicon nitride and silicon oxide, and are batch fabricated using microfabrication techniques. Typical length, width, and thickness of microcantilevers used in AFM are 100, 10, and 2 μm, respectively. The stiffness of the microcantilever can vary from 0.06 to 100 N/m [6].

A typical AFM setup is shown in Figure 2. The prevalent method for measuring the cantilever deflection uses a laser beam, which is focused on the cantilever and is reflected from the cantilever surface into a split photodiode. The cantilever deflection changes the angle that the incident laser beam makes with the cantilever surface, which, in turn, changes the incidence position on the photodiode, which is registered as a change in the photodiode voltage. The length of the reflected laser path amplifies the cantilever deflection.

The fixed end of the cantilever is supported by the *base*, which is typically attached to a *dither piezo* (Figure 2). The dither piezo provides a means for oscillating the base of the cantilever. A scanner, which is actuated by piezoelectric material, positions the sample laterally and vertically during imaging.

Cantilever Model

The cantilever is a flexure member whose first mode is described by the spring-mass-damper dynamics

$$\ddot{p} + \frac{\omega_0}{Q}\dot{p} + \omega_0^2 p = f(t), \tag{2}$$

$$y = p + \upsilon, \tag{3}$$

where p, f, y, and υ denote the deflection of the tip, force on the cantilever, measured deflection, and measurement noise, respectively, whereas the parameters ω_0 and Q are the first modal frequency (resonance frequency) and quality factor of the cantilever. The quality factor characterizes the energy loss of the cantilever to the surrounding environment. The first modal frequency of typical cantilevers used in AFM are in the range 10–400 kHz, while Q can range from 2 in a liquid environment to 10,000 or higher under vacuum. The measurement noise υ is dominated by 1/f noise at low frequencies and is nearly white at frequencies beyond a few kilohertz. The cantilever model (2) can be identified precisely [7]. Viewing the cantilever as a filter (2) proves crucial for employing systems and control perspectives to AFM.

Tip-Sample Interaction Model

The interaction force between the tip and the sample can be characterized by the Lennard-Jones force

$$F(r) = -\frac{6A}{r^7} + \frac{12B}{r^{13}}, \tag{4}$$

where r is the separation between the tip and the sample [Figure 3(b)]. The term $-A/r^7$ models the Van der Waals interaction that characterizes the attractive force between the atoms of the tip and the sample. The effect of these long-range forces is perceptible when two atoms are separated by distances smaller than 10 nm. At separations smaller than 1 Å, the overlap of electron clouds and ionic interactions causes strong repulsive forces between atoms on the cantilever and atoms on the sample surface. The effect of the repulsive forces is captured by the term B/r^{13} in the Lennard-Jones model. This model provides a good qualitative characterization of the tip-sample interaction, notwithstanding the diverse factors that cause experiments in AFM to deviate from this model. A detailed analysis of various surface interactions is given in [8].

Force Curves

The photodiode sensitivity characterizes the change in the voltage registered at the photodiode for a given change in the cantilever deflection. This factor depends on the incidence angle of the laser with the cantilever surface and, therefore, changes every time a new cantilever is used. The *force curve*, which is the plot of photodiode measurement versus tip-sample offset, provides a means to calibrate the photodiode sensitivity. Figure 3 describes the interaction of an atom on the tip of the cantilever with an atom on the surface of the sample. For illustration, consider the dynamics of a cantilever with stiffness k and unit mass under the influence

of a tip-sample interaction force modeled by the Lennard-Jones force given by (4).

In the development below, we set the equilibrium position that the cantilever assumes in the absence of the sample to the zero reference position [Figure 3(a)]. The cantilever deflection p is taken as positive when the tip displaces away from the sample. The *offset* ℓ of the base of the sample from the reference position can be changed by moving the sample vertically toward or away from the cantilever base by actuating the piezo positioner. The separation r between the tip and the sample atoms is given by $r = \ell + p$. The equation of motion for the cantilever deflection is given by

$$\ddot{p} = F(p, \ell) - kp,$$

while the equilibrium points of the dynamics are obtained from $\dot{p}_{\text{eq}} = 0$ and $F(p_{\text{eq}}, \ell) = kp_{\text{eq}}$.

In terms of the separation r, the equilibrium points are characterized by the intersection of the curves $k(r - \ell)$ and $F(r, \ell)$ as functions of r [Figure 3(b)]. For a given value of ℓ, an equilibrium point $p_{\text{eq}} = r_{\text{eq}} - \ell$ is unstable if the slope

$$\left.\frac{\partial F(p, \ell)}{\partial p}\right|_{p = p_{\text{eq}}} = \left.\frac{\partial F(r, \ell)}{\partial r}\right|_{r = r_{\text{eq}}} > k, \qquad (5)$$

that is, if the slope of the straight line that characterizes the spring force is smaller than the slope of the curve $F(r, \ell)$ at the equilibrium point. For the value of the offset ℓ shown in Figure 3(b), the dynamics have three equilibrium points e_1, e_2, and e_3, of which e_1 and e_3 are stable, whereas e_2 is unstable.

In the approach phase of the force curve, the tip-sample offset ℓ is reduced quasi-statically by slowly moving the sample closer to the surface. The change in the equilibrium position due to a reduction in the offset ℓ can be evaluated by translating the line representing the spring force to the left [Figure 3(b)]. When ℓ is large, a unique equilibrium point occurs in the attractive portion of the tip-sample interaction. This equilibrium point is represented by A in Figure 4. As ℓ is reduced, the equilibrium point moves along the Lennard-Jones curve from B to C. Further reduction of ℓ results in both an unstable equilibrium point C in the attractive portion and a stable equilibrium point D in

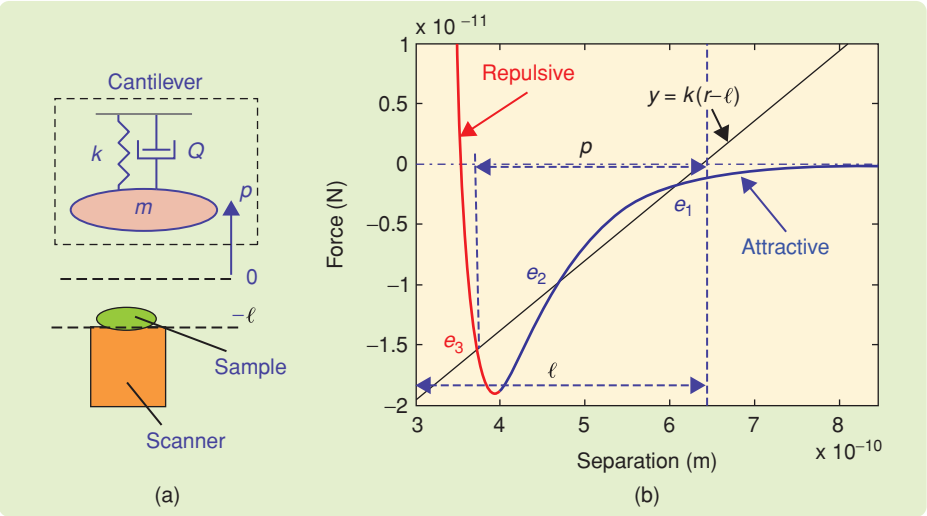

FIGURE 3 (a) Reference system and (b) equilibrium points. In (a), a spring-mass-damper model of the cantilever and reference frame are illustrated. The equilibrium position that the cantilever assumes in the absence of the sample defines the zero reference position. Displacements above the reference position are considered positive. The deflection of the cantilever is p, while the sample is at $-\ell$, where ℓ is the offset. The offset ℓ can be changed by actuating the piezo positioner that holds the sample. The separation between the sample and cantilever atoms is given by $r = \ell + p$. In (b), the equilibrium points of the cantilever for a given value of ℓ are determined by the intersection of the line $k(r - \ell)$ and the Lennard-Jones curve. Equilibrium points e_1 and e_3 are stable, whereas e_2 is unstable. The deflection p of the cantilever is shown in (b) for the case in which the cantilever assumes the equilibrium position e_3.

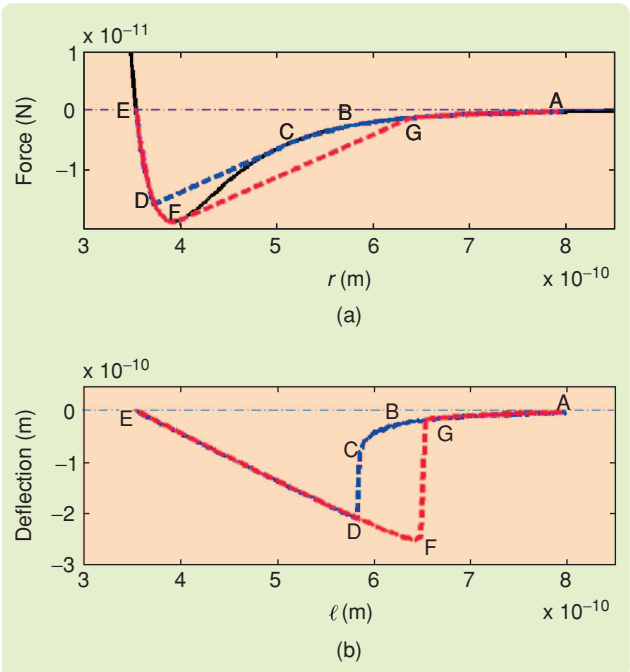

FIGURE 4 (a) Force versus separation in the approach phase and the retract phase and (b) deflection versus offset in the approach phase and and the retract phase of a force curve. The deflection p of the cantilever in the approach phase and the retract phase is given by the curves ABCDE and EDFGA, respectively. Part (a) shows the force versus separation r curve, whereas (b) shows the corresponding cantilever deflection p versus offset ℓ curve. The hysteretic nature is evident in both curves. The goal is to reconstruct the force versus separation curve from the deflection versus offset curve, which can be determined from experimental data.

the repulsive portion of the tip-sample interaction. The cantilever tip cannot assume an unstable equilibrium point and therefore jumps into the repulsive region to the stable equilibrium point D, that is, the tip snaps into contact with the sample. As the offset ℓ is decreased, the equilibrium point traverses the repulsive portion of the tip-sample interaction along the Lennard-Jones force curve from D to E.

At the end of the approach phase, the sample is retracted, and the tip retraces the repulsive region explored in the approach phase from E to D. At a value of ℓ corresponding to F, the tip jumps into the attractive region at G. This jump in the retract phase occurs at a value of ℓ that is different from the value of ℓ corresponding to the jump in the approach phase, leading to a hysteretic feature on the force curve. An interesting observation is that when the cantilever is in the repulsive phase, the ratio of the change in deflection to the change in ℓ is approximately unity since the strong repulsive force makes the cantilever tip move approximately the same distance as the sample. This observation forms the basis for calibrating the photodiode. The motion $\Delta\ell$ of the sample is derived from both the voltage V_{piezo} applied to the piezo scanner and the piezo sensitivity, which determines the distance in nanometers that the scanner moves vertically for each volt applied to the piezo. The photodiode sensitivity is determined by inverting the slope of the line obtained by plotting the photodiode against the offset ℓ in the repulsive phase.

The force curve is the plot of the cantilever deflection versus the offset ℓ in the approach and retract phases. Some applications require evaluation of the tip-sample force profile from the deflection-separation curves. Force-curve data provide one of the primary AFM methods for unraveling intermolecular force landscapes of biomolecules.

Thermal Noise

In thermal equilibrium, the cantilever is forced by *thermal noise*, a white noise that causes the cantilever to deflect in a random manner. The transfer function from thermal noise η to the cantilever deflection p is given by

$$G(s) = \frac{1}{s^2 + \frac{\omega_0}{Q}s + \omega_0^2}. \tag{6}$$

In typical AFM setups, the measurement noise and thermal noise are such that the response of the cantilever to the thermal noise forcing is evident only near the resonance frequency of the cantilever [Figure 5(a)]. Away from the resonance frequency, the measurement noise dominates the cantilever deflection due to the thermal noise. At low frequencies (near dc), $1/f$ noise dominates the spectrum. In contrast to typical sensors, where noise sources other than thermal noise dominate the spectrum, in AFM, the thermal response of the cantilever dominates other noise sources near the resonance frequency of the cantilever. The cantilever probe is thus thermally limited near the resonance frequency of the cantilever.

The thermal noise response of the cantilever provides a convenient and elegant way of calibrating the cantilever. By using the power spectral density near resonance, the stiffness k, quality factor Q, and resonance frequency of the cantilever can be obtained (see [7] for a multimode fit).

The cantilever experiences the thermal noise force η, tip-sample interaction force h, and dither force $g(t)$, which is provided by the dither piezo (Figure 2). The transfer function of the cantilever is defined in (6), which maps the input

$$f = g + h + \eta \tag{7}$$

to the output

$$p = Gf, \tag{8}$$

which results in the measurement

$$y = p + \upsilon = G(g + h + \eta) + \upsilon, \tag{9}$$

where υ is the measurement noise introduced by the laser and photodiode arrangement (Figure 2).

PREVALENT MODES OF AFM OPERATION

The AFM is used in various operating modes depending on the pertinent application. These operating methods can be broadly classified as *static* or *dynamic*.

Static Mode Operation

In the static mode operation of the AFM, the base of the cantilever is not forced. In this mode, since the measurement is broadband, the $1/f$ noise affects the detection scheme and plays a critical role in determining the imaging resolution [6]. For meaningful imaging, the deflection of the cantilever has to be larger than the root mean square (rms) deflection of the cantilever due to the dominant noise source. The response of the cantilever due to thermal noise in this mode is dominated by the measurement noise, and thus does not determine the imaging resolution. The deflection of the cantilever caused by the force on the cantilever tip due to the sample has to overcome the large measurement noise. Since the interaction forces between the tip and sample are small, the cantilever stiffness must be small to facilitate a sufficiently large deflection to overcome the measurement noise. From the above discussion on force curves, it is evident that the equilibrium points on the attractive portion of the tip-sample interaction are unstable for soft cantilevers. Thus, the operating condition of static mode methods is restricted to the repulsive portion of the force curve, where the forces on the tip and sample are larger.

The most prevalent static mode operation of the AFM is the constant-force mode, where the *force balance* principle is used. The piezoactuated scanner moves the sample in the lateral x-y directions while simultaneously positioning the sample in the vertical z direction through a controller to maintain a constant photodiode voltage, or, equivalently, a fixed cantilever deflection. A constant cantilever deflection p_0 indicates that a constant force kp_0 is applied to the cantilever. In this mode, the z-control signal gives a measure of the height of the topographic feature on the sample, while the lateral x-y coordinates of the feature are given by sensors of the lateral positioning system. Thus, the image of the sample topography is obtained by plotting the z-control signal against the lateral x-y coordinates.

The advantages of this method are the ease of data interpretation and the ease of implementation. A severe drawback of this mode is that it cannot be used on soft samples, which can be damaged due to large vertical and lateral tip-sample forces that arise as the tip drags on the sample. As a consequence, AFM imaging of biological matter usually employs the dynamic mode operation.

Dynamic Mode Operation

The deflection measured by the photodiode is given by (9). Figure 5(a) shows an experimentally obtained power-spectral density of the measured deflection signal y when the force on the cantilever is the thermal noise force η. It is evident from Figure 5(a) that the characteristics of G are visible near the resonance of the cantilever, whereas, away from the resonance frequency, the measurement noise clouds the thermal noise response $G\eta$ of the cantilever. We note that, at a given temperature, thermally limited resolution is the best achievable resolution. When the signal of interest, for example, topography of the sample, is modulated such that required information is present near the resonance frequency of the cantilever, the measurement benefits from the high signal-to-noise ratio (SNR). In dynamic methods, the modulation is achieved by oscillating the cantilever sinusoidally at a frequency close to its resonance frequency by forcing the base with a dither piezo (Figure 2). The changes in the cantilever oscillations due to the interaction with the sample are monitored to infer sample properties. The effect of the sample on the cantilever is typically modeled as a change in the resonance frequency and damping of the cantilever. This viewpoint is explained by modeling the cantilever as a beam fixed at one end with the sample force acting on its free end, that is, the end with the tip. The boundary condition at the free end determines the resonance frequency of the cantilever, while the change in the damping factor of the cantilever is due to the energy losses caused by the interaction with the sample.

Dynamic mode operations are explained by comparing the frequency responses of the cantilever with and without

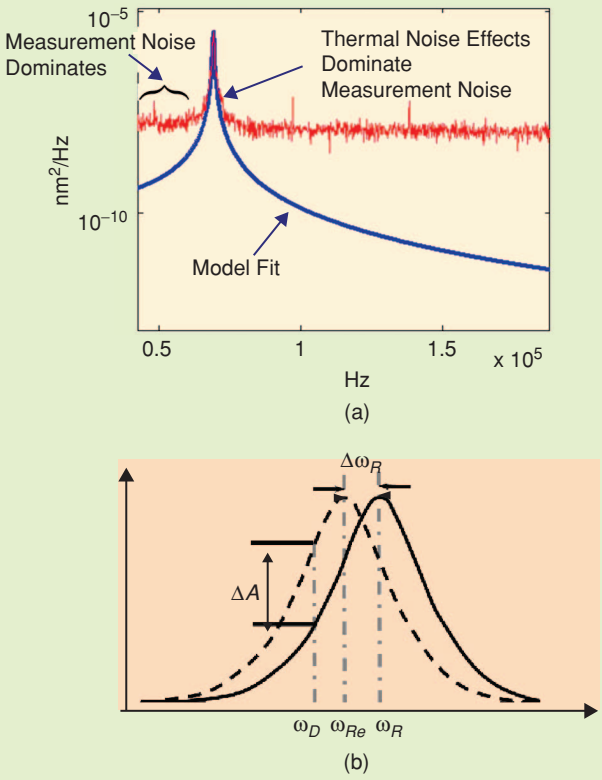

FIGURE 5 (a) Effect of thermal noise on the cantilever deflection and (b) effect of the sample on the frequency response of the cantilever. The experimental thermal noise plot shown in (a) shows that, in the low-frequency region, the measurement noise dominates the thermal noise response of the cantilever. At and near resonance, the thermal noise response dominates the measurement noise. The second-order model fit provides an estimate of the spring constant of the cantilever. In (b) the cantilever under the influence of the sample is modeled as an equivalent spring-mass-damper system with a changed resonance frequency ω_{R_e} with the original resonance frequency of the cantilever given by ω_R. The cantilever is forced with a drive frequency ω_D.

the influence of the sample [Figure 5(b)]. When the cantilever is not under the influence of the sample, a sinusoidal forcing with magnitude γ and frequency ω_D results in a deflection signal that is sinusoidal with amplitude A. In the absence of the sample, the resonance frequency of the cantilever is ω_R. Under the presence of a sample, which causes an attractive force on the cantilever, the amplitude-frequency curve shifts to the left with a reduced resonance frequency ω_{R_e} and an increased amplitude $A + \Delta A$. The shift ΔA in the amplitude is exploited by the amplitude modulation AFM (AM-AFM) method to measure the sample interaction. In frequency modulation AFM (FM-AFM), the difference $\Delta\omega_R$ between the *equivalent resonance frequency* ω_{Re} of the cantilever under the sample influence and the *free resonance frequency* ω_R is used to map the sample characteristics.

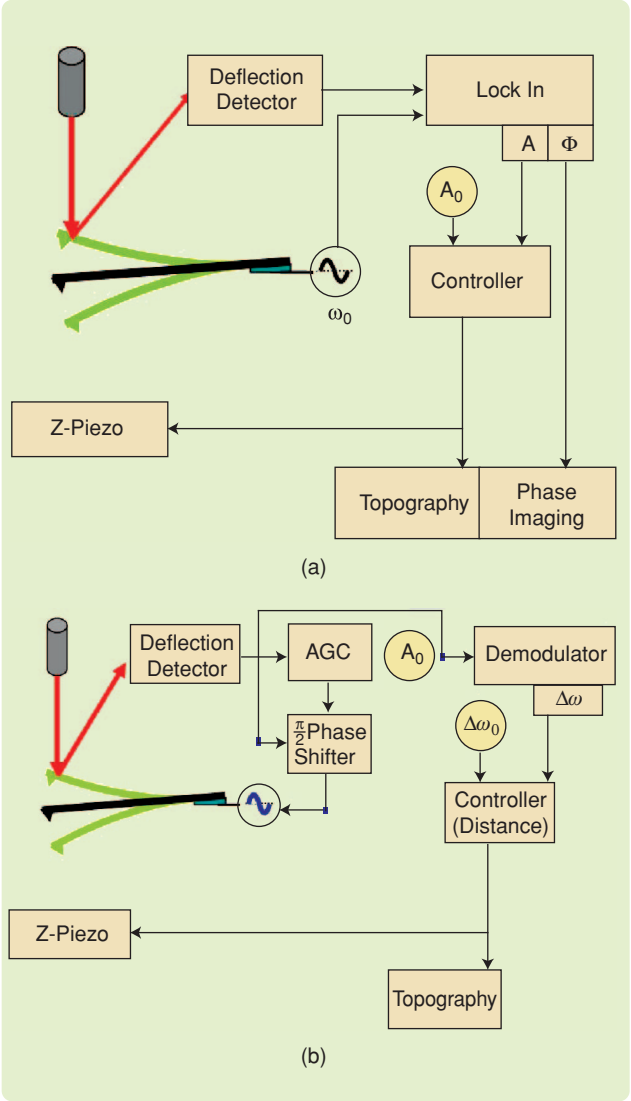

FIGURE 6 (a) Amplitude modulation atomic force microscopy (AM-AFM) and (b) frequency modulation atomic force microscopy (FM-AFM). In the AM-AFM scheme, the cantilever is forced sinusoidally by the dither piezo at or near the resonance frequency of the cantilever. The amplitude A and the phase Φ of the first harmonic of the cantilever oscillation are determined from the cantilever deflection. The controller uses the Z-piezo to position the sample vertically to maintain the setpoint amplitude A_0. In the FM-AFM method, the equivalent resonance frequency is measured, and the shift $\Delta\omega$ of this frequency from the free resonance frequency is determined. The controller uses the Z-piezo to position the sample vertically to maintain a setpoint frequency shift ω_0. The cantilever is forced by the dither piezo at the equivalent resonance frequency by maintaining the forcing at a phase shift of $\pi/2$ rad with respect to the first harmonic of the deflection. The amplitude is maintained at a set value A_0 by an automatic gain controller (AGC).

AM-AFM

In AM-AFM, the cantilever is forced sinusoidally at its first modal frequency [Figure 6(a)]. The sinusoidal oscillation of the cantilever changes when it interacts with the sample. The cantilever oscillations are bandpass filtered with center frequency ω_0. The amplitude A and phase ϕ are retrieved by obtaining the in-phase and quadrature components of the cantilever oscillation. The amplitude A is provided to the controller, which regulates a setpoint amplitude A_0 by moving the sample using a piezo-positioner. The control signal that regulates the setpoint amplitude provides a measure of the sample topography. In contrast to static mode imaging, in this intermittent contact method, the tip explores the sample only once every period, which leads to less wear and tear of the tip and the sample. Typical amplitudes of oscillations are in the 2–50 nm range, of which the tip-sample interaction is effective over 0–10 nm. AM-AFM is used to image samples that have relatively large (tens of nanometers) topographic variation. Furthermore, AM-AFM operation is robust and well suited for operation under fluids, in particular, for imaging biosamples.

In AM-AFM, the SNR can be increased by using a higher quality-factor cantilever. However, a lower damping coefficient results in a small imaging bandwidth. For example, although a quality factor Q greater than 50,000 offers excellent sensitivity, the associated bandwidth is less than 1 Hz, which is too slow for practical use.

Frequency Modulation AFM

The FM-AFM mode provides increased sensitivity through the use of higher quality-factor cantilever without compromising bandwidth [9]. In this method, the cantilever is made to oscillate at the equivalent resonance frequency by regulating a $\pi/2$-rad phase offset between its oscillations and the sinusoidal drive to the cantilever [Figure 6(b)]. The demodulation of the cantilever deflection signal yields the equivalent resonance frequency. In this mode, the measurement bandwidth does not degrade when Q of the cantilever is increased. The controller regulates a reference frequency shift $\Delta\omega_0$ by comparing it with the measured frequency shift $\Delta\omega$. The Z-piezo positions the sample according to the error in the desired and measured frequency shifts. This scheme is limited by thermal noise and therefore enables imaging with high resolution; however, the stiffness k, amplitude of oscillation A, and quality factor Q need to be large to ensure successful operation. This scheme is typically operated under ultrahigh vacuum and low-temperature conditions and works well for samples that have small variation in topography [9].

NEEDS AND CHALLENGES

In this section we briefly describe the challenging demands imposed on future generation SPMs. These demands can be broadly classified as follows.

High-Resolution Needs

To investigate matter at the atomic scale, subangstrom resolution is needed. Such high-resolution imaging is crucial to obtaining a fundamental understanding of nanoscale processes and for testing hypotheses on the interaction of

matter at this scale. Subatomic-scale resolution results, though rare, are obtained by employing microcantilevers under ultrahigh vacuum and low-temperature conditions [10], [11]. A severe drawback of investigating matter under these conditions, besides the high cost and complexity of the experimental setup, is that the behavior of matter under vacuum and low temperatures can be substantially different from the behavior under normal conditions. Thus, high-resolution imaging under ambient conditions is necessary to open up new avenues for studies in nanoscience. However, the associated uncertainties due to high-temperature operation and a contaminated environment due to lack of high vacuum are significant, which makes the task of obtaining atomic-scale resolution challenging.

High-Bandwidth Needs

Pivotal to harnessing the vast potential of nano-investigation is the ability to interrogate at high speeds. This need arises from the requirement for probing sample features that have subnanometer dimensions over areas that have macroscopic dimensions. This range of scales necessitates large throughput rates to enable interrogation of practical-sized samples with characteristic dimensions in the 1-μm to 1-mm range. The usual approach is to reduce device dimensions to enhance the associated resonance frequencies, thereby facilitating higher bandwidth operations [12]. The fundamental drawback of this approach is the limitation on the sample size that can be accommodated, for instance, the device described in [12] cannot be used for samples larger than 250 nm $\times$ 250 nm. The need for specialized fabrication techniques is another deterrent to this approach. A new paradigm must be developed to attain ultrahigh bandwidth without sacrificing sample size.

Interpretability

A fundamental issue in investigating matter at the nanoscale is that the observation process itself can affect the matter being investigated, which further motivates the use of minimally invasive interrogation schemes. Even when the interrogation is noninvasive, the material characteristic being sought must be gleaned from measured data. Typically, the probe introduces artifacts due to its dynamics. Artifacts introduced by the probe must therefore be properly accounted for.

SYSTEMS AND CONTROL APPROACHES

We now demonstrate how control-system viewpoints partially address the challenges mentioned above.

Feedback Model of Tip-Sample Interaction

The system described by (2) with f given by (7) can be viewed as an interconnection of a linear system and a nonlinear system as depicted in Figure 7, where $h = \phi(p)$ is the sample force per unit mass. The forcing g is assumed to be sinusoidal with period $2\pi/\omega_0$. The tip-sample interaction force appears as a feedback block. The AFM dynamics are viewed as an interconnection of two systems, namely, the system G, which models the cantilever, and the block ϕ, which models the tip-sample interaction.

This systems perspective of a Lurè system is used in [13] and [14] to study dynamic mode operation of AFM using harmonic and power balance tools. In [15], this viewpoint is employed to study the bounds on harmonics of the dynamic mode operation. The hysteretic behavior of the dynamic mode force curves is analyzed in [16] using a piecewise linear model of the tip-sample interaction potential.

Analysis based on systems and control approaches as well as experimental studies on tip-sample interactions demonstrate complex dynamics that arise in dynamic mode operation. Complex dynamics often manifest themselves as abrupt changes in the qualitative behavior of the dynamics, which can be used to provide improved resolution [17], [18]. For instance, [17] considers a setup in which the sample is oscillated at various frequencies and amplitudes with the cantilever held stationary. In experiments, it is observed that, as the amplitude of oscillation is increased, the power spectral density of the cantilever deflection shows a succession of subharmonics. This observation is predicted by the theoretical model developed in [17], which establishes existence of chaotic orbits by the way of period doubling.

Thermally Driven Noncontact Atomic Force Microscopy

In many studies, minimally invasive investigation of tip-sample interaction forces at room temperature is of interest. Relevant applications include noninvasive detection of the motion of the cell surface [19]. In such studies, the detection of localized forces requires tip-sample separations in subnanometer scales, which must be maintained for extended periods of time. This requirement is either imposed by the time scales of the dynamic process being studied or arises from the need to achieve a specified sensitivity.

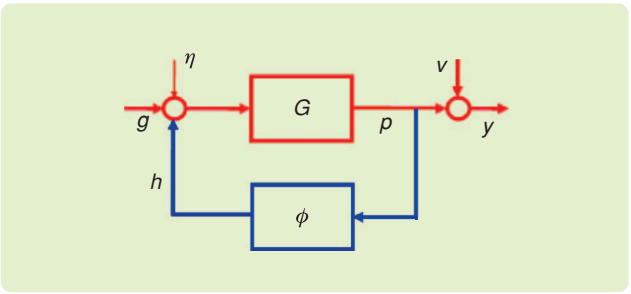

FIGURE 7 A feedback representation of the atomic force microscope dynamics. The cantilever-sample system is considered as the feedback interconnection of a linear system G with a static nonlinearity ϕ. The tip-sample interaction force per unit mass h is a function of the cantilever position p, that is, $h = \phi(p)$. The forcing on the cantilever through the dither piezo, thermal noise, and sensor noise are represented by g, η, and v, respectively.

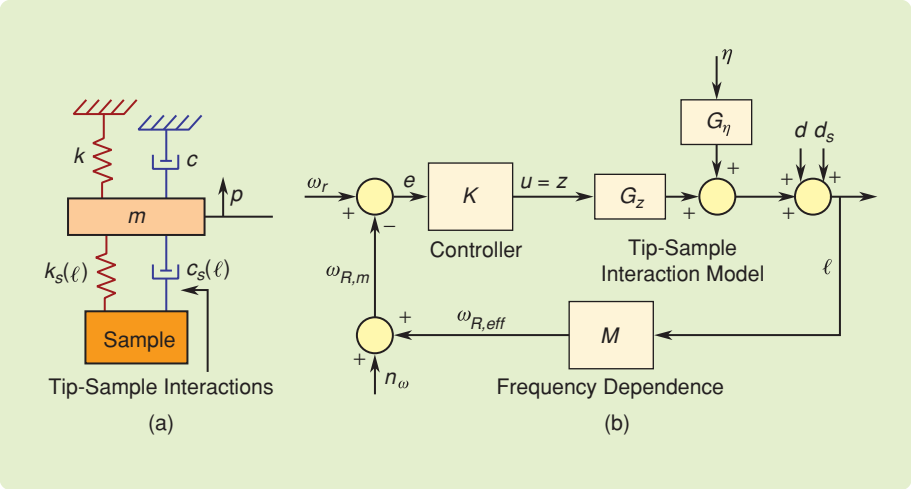

FIGURE 8 (a) Model for the cantilever-sample system and (b) systems view of thermally driven noncontact atomic force microscopy. The sample influence can be modeled by a spring k_s and a damping mechanism. The combined system has a stiffness that is less than the free cantilever stiffness k, and has a resonance frequency that is different from the free resonance frequency. When the cantilever is in the attractive portion of the interaction, k_s is negative, whereas, when the cantilever is in the repulsive portion, k_s is positive. Correspondingly, the equivalent resonance frequency satisfies $\omega_{R,\text{eff}} < \omega_0$ in the attractive portion and $\omega_{R,\text{eff}} > \omega_0$ in the repulsive portion of the tip-sample interaction. In (b) the transfer function G, which refers to the cantilever interacting with the sample, consists of the transfer functions $G_z(s)$ and $G_\eta(s)$. $G_z(s)$ accounts for the dependence of the tip-sample separation p on the sample position z, while $G_\eta(s)$ represents the effect of thermal noise η, which is modeled as white noise, on p. $M(s)$ represents the dependence of $\omega_{R,\text{eff}}$ on p. $K(s)$ is the feedback control law actuating the z motion of the sample by means of the control output u, in an effort to maintain the measured resonance frequency ω_m at the desired value ω_r. The term n_ω represents the noise in the frequency estimation. The effect of the drift processes is modeled as a disturbance d in the sample position. The sample deformation is shown as d_s.

Main Concept

In the thermally driven noncontact AFM (ThNcAFM) imaging method, the cantilever tip is maintained in the attractive portion of the tip-sample interaction potential by using the thermal response of the cantilever to distinguish the attractive portion from the repulsive portion. The attractive portion of the tip-sample potential is the desirable region for positioning the tip to investigate the sample characteristics since this region is neither too far for the effects of the sample to be negligible nor too close to be in the repulsive portion, where the tip can be invasive. The effective spring constant k_{eff} and the resonance frequency $\omega_{R,\text{eff}}$ of the cantilever decrease when the cantilever is in the attractive portion of the tip-sample interaction and increase when the cantilever is at the repulsive portion. In ThNcAFM, the shift in the resonance frequency in thermal-noise response of the cantilever deflection is monitored to maintain the cantilever in the attractive portion. The effective resonance frequency is determined by noting the peak in the power spectral density of the deflection signal of the cantilever, which is forced by the thermal noise. Thus, without introducing external forcing to the cantilever and by using its thermal response, ThNcAFM discerns whether the tip is in the attractive or the repulsive portion of the tip-sample interaction.

The drift processes, which are caused by various factors such as temperature changes, relaxation processes, and piezo-crystal-related effects, move the tip away from the attractive portion of the tip-sample interaction. In ThNcAFM, the equivalent frequency of the cantilever estimated from the thermal response data is compared to a reference frequency, and the sample's position is changed to regulate the equivalent resonance frequency. This feedback scheme counteracts the drift effects and maintains a constant tip-sample separation by regulating an equivalent reference resonance frequency of the cantilever. The associated framework is described in Figure 8. The transfer functions $G_z(s)$, $G_\eta(s)$, and $M(s)$ shown in Figure 8 represent the dependence of the tip-sample separation p on the sample position z, the effect of the thermal noise η on p, and the dependence of $\omega_{R,\text{eff}}$ on p, respectively. The feedback control law $K(s)$ actuates the z-motion of the sample through the control output to maintain the equivalent resonance frequency at the desired value ω_r. To estimate the effective resonance frequency, the thermal noise response is modeled as the sum of a single sinusoid and white noise. The frequency of the sinusoid, corresponding to the effective resonance frequency of the cantilever, is estimated by Pisarenko harmonic decomposition [20]. The term n_ω represents the noise in the frequency estimation. In ThNcAFM, the driver is the thermal noise forcing, and, therefore, the SNR is close to unity. Thus, in contrast to classical dynamic methods, where the cantilever is driven, n_ω is large, leading to a small SNR. The reference frequency ω_r is chosen to be below the natural resonance frequency ω_0. This choice of reference frequency maintains the cantilever in the attractive portion of the tip-sample interaction. The drift processes d are slow, and the controller K is designed to reject the disturbance d. The low-frequency content of d makes it possible for the controller to be effective even though the measurement noise n_ω is large. The closed-loop bandwidth is designed such that disturbance d is filtered by the control loop, and the effect of sample deformation d_s is discerned from the corresponding variations in $\omega_{R,\text{eff}}$.

In ThNcAFM, the rms amplitude of the cantilever deflections at a given temperature T is given by $\langle A^2\rangle^{1/2} \approx k_B T/k$, where k_B is the Boltzmann constant and k is the stiffness of the cantilever. When the oscillations of the cantilever have small amplitudes, the resonance shift due to conservative tip-sample forces is closely approximated by $\Delta\omega_R \approx \omega_R(k_s/2k)$, where $\omega_R = \omega_0\sqrt{1-(1/4Q^2)}$ is the cantilever's resonance frequency and k_s is the local tip-sample force gradient. Unlike classical methods with large amplitudes ($A \approx 5$–80 nm), data interpretation is relatively straightforward. Large-amplitude methods [9] also suffer from limited sensitivity to short-range forces and, therefore, do not yield atomic-scale resolution. The small-amplitude operation with amplitudes on the order of subangstroms is recommended [21] for improved sensitivity to short-range forces. The small-amplitude method with the cantilever forced near its free resonance frequency is discussed in [22]. Since the quality factor Q is high, it is difficult to produce small oscillations near the resonance frequency of the cantilever. Resonance frequency modulation experiments employing small amplitudes are considered in [10] and [11]. Small amplitudes of the cantilever oscillations can be generated by forcing the cantilever away from its resonance frequency [23]–[27]. However, off-resonance AM techniques and low-Q cantilevers compromise the resonance enhancement to sensitivity and lead to lower imaging resolution.

ThNcAFM exploits the thermal forcing of the cantilever, thereby obviating the external positive-feedback excitation used in classical FM-AFM methods and the associated feedback stability issues. Furthermore, the amplitudes realized in ThNcAFM are the smallest possible at a given temperature, since the thermal drive is the smallest possible drive. ThNcAFM thus provides the advantages of small-amplitude methods. Additionally, the broadband nature of thermal forcing yields information at frequencies away from resonance. For ThNcAFM, the power of the frequency noise is given by $\sqrt{\omega_0 B/Q}$, where B is the measurement bandwidth, which is independent of the temperature. This temperature independence of the frequency noise is potentially useful for applications that require elevated temperatures.

In ThNcAFM, bandwidth needs are compromised due to the large noise present in estimating the equivalent resonance frequency. This method is useful for studying persistent sample behavior. The promise of high resolution is realized by maintaining the cantilever probe in the attractive portion of the tip-sample interaction potential for long periods of time (>30 min). A long observation time allows for the noise to be averaged and the subangstrom sample dynamics to emerge. The ability to position the cantilever at nanometer separation for long periods is thus an enabling tool for nanotechnology applications such as monitoring the dynamics of biomolecules.

Experimental Results

Figure 9 shows the experimentally observed variation in the cantilever resonance frequency as a function of tip-sample separation during approach and retraction. It is seen that the resonance frequency decreases due to the long-range attractive tip-sample interactions. In these experiments, $T = 300$ K, $Q = 450$, $k = 1$ N/m, $\omega_0 = 2\pi \cdot 350 \times 10^3$ rad/s, the rms amplitude is $\langle A^2\rangle^{1/2} \approx 0.64$ Å, and the theoretical frequency noise density is 489 Hz^2/Hz. The measured cantilever resonance frequency is shown in Figure 10(a), where the controller maintains a reference resonance frequency. In the initial stages of the experiment, the tip is not interacting with the sample, and the measured resonance frequency is 353.6 kHz. Once the desired tip-sample separation is achieved, as indicated by the resonance frequency being close to the reference 353.2 kHz, the control action counteracts the drift in the instrument. At approximately 1500 s into the experiment, a step change in the reference is introduced, and the controller tracks this change. Note that the equivalent resonance frequency of the controller is maintained below its natural frequency for more than 30 min, indicating that the cantilever tip is in the attractive regime during this time. In Figure 10(b), which demonstrates the significance of ThNcAFM, the sample is oscillated at 250 Hz with amplitudes as small as 0.125 Å. Oscillations with amplitudes as small as 0.25 Å are detected in the power spectral density plots of the estimated equivalent frequency.

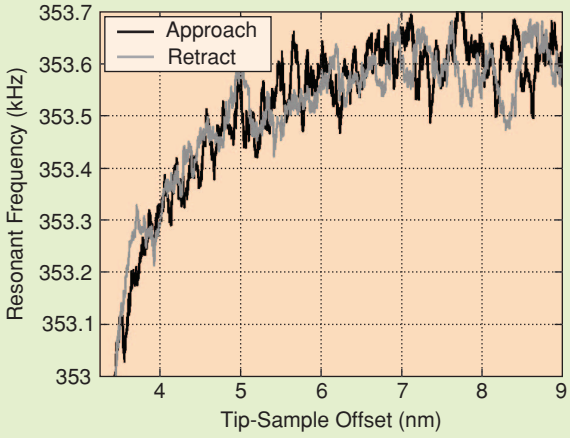

FIGURE 9 Estimates of the equivalent resonance frequency of the cantilever by thermal spectra at various tip-sample offsets. In the approach phase the cantilever and sample are brought closer by reducing the offset, whereas in the retract phase the offset between the cantilever and the sample is increased. The decreasing trend in the resonance frequency with respect to the offset is evident in both phases. The tip interacts increasingly with attractive potential as the sample is brought closer to the cantilever tip.

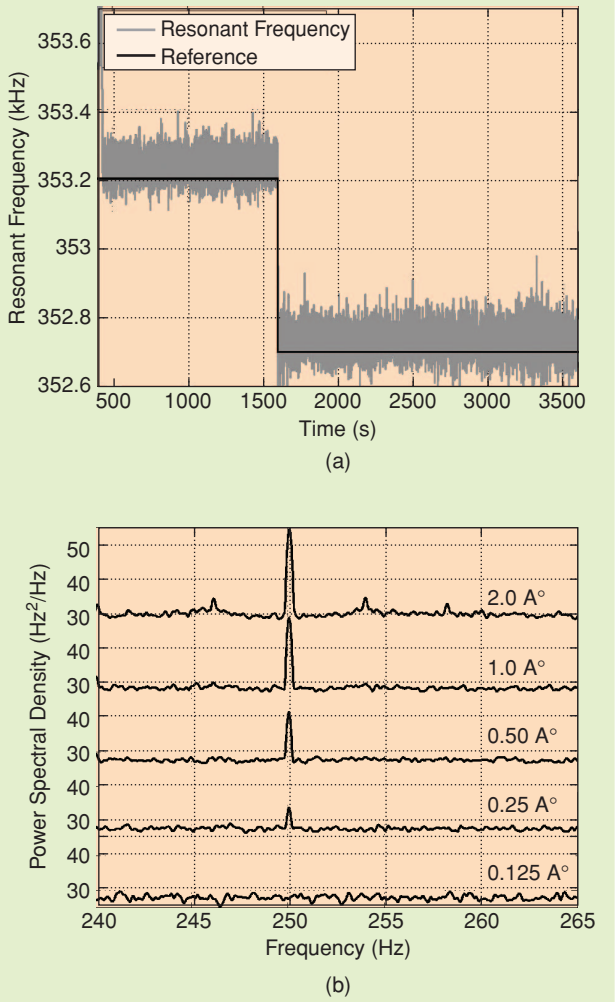

FIGURE 10 (a) Feasibility of controlling tip-sample separation in thermally driven noncontact atomic force microscopy and (b) resolution of thermally driven noncontact atomic force microscopy. Part (a) demonstrates that the cantilever tip can be controlled to remain in the attractive portion of the tip-sample interaction for long periods of time. The free resonance frequency of the cantilever is 353.6 kHz. The cantilever tip is maintained in the attractive portion of the tip-sample interaction by regulating the reference frequency to 353.2 kHz. At approximately 1500 s, a step change in the reference is introduced, and the cantilever tracks this change. Part (b) demonstrates that subangstrom resolution is obtained in air. The sample is oscillated at 250 Hz at various amplitudes ranging from 2 Å to 0.125 Å. Sample oscillations as small as 0.25 Å are detected, as indicated by the peak at 250 Hz.

Transient-Force Atomic Force Microscopy

Although mathematical models of AFM are used for describing and analyzing experimental observations, they are rarely used in experiments to enhance device performance. In [28], transient force AFM (TF-AFM) demonstrates the potential of using models in real time, where experimental results confirm detection rates of two orders higher than prior methods.

Main Concept

For dynamic-mode AFM applications, a single-mode model often suffices to capture the cantilever dynamics as in (2) with f given by (7). Typically, the cantilever is externally driven by a sinusoidal force $g(t) = \sin \omega t$, where ω is approximately equal to the free resonance frequency ω_0. When η is ignored, the solution to (2) when $f(t) = g(t) = \gamma \sin \omega_0 t$ is of the form

$$p(t) = \underbrace{A_0 \sin(\omega_0 t + \nu_0)}_{\text{steady state}} + \underbrace{A' e^{-\frac{\omega_0 t}{2Q}} \sin(\omega' t + \nu')}_{\text{transient}}, \qquad (10)$$

where $\omega' = \omega_0\sqrt{1 - 1/4Q^2}$ and with ν' and A' determined by the initial conditions $p(0)$ and $\dot{p}(0)$ of the cantilever. Since the transient term decays as $e^{-(\omega_0 t/2Q)}$, the settling time is roughly Q cycles of cantilever oscillations. This dependence on the quality factor Q suggests a limitation on bandwidth for imaging since high Q, with values in the range 100–50,000, is necessary for high resolution. This dependence on quality factors can be explained by the following hypothetical experiment. Imagine the cantilever is in steady state, oscillating freely without interacting with the sample. Suppose a sample feature perturbs the cantilever's motion, and the cantilever eventually returns to a steady state. The interaction with the sample is manifested as a position and velocity reset in the cantilever model, which results in a transient term as described in (10), which dies out in Q cycles. To ensure that the effect on the cantilever's motion from a sample feature does not corrupt the measurement signal from a subsequent sample feature, the cantilever must sense the features at time intervals that are separated by at least Q cycles. This condition on temporal separation between features imposes severe limitations on the scanning bandwidth, which in some applications are impractical.

Note, however, that after the first feature stops interacting with the cantilever, the cantilever motion is accurately described by (9) with no sample force, that is, with $h = 0$. An observer M (Figure 11), when designed with the cantilever model parameters k, m, and Q and provided with the sinusoidal dither forcing g as well as the measurement y, can estimate the cantilever state. M tracks the cantilever state, even when the transient term is present as long as M uses the correct model of the cantilever. Also, how well and how fast the observer M tracks the cantilever position and velocity depends primarily on the photodiode noise, which can limit the observer gain. Since the measurement noise is small ($\approx 0.1\ \text{nm}/\sqrt{\text{Hz}}$), the choice of the observer gain is practically unconstrained. The number N of periods of the cantilever oscillation that the observer takes to track the cantilever state does not depend on the quality factor Q; for typical measurement noise, N is approximately equal to four [29]. The mismatch between the position

estimate $\hat{y}_1$ and the cantilever measured output y is significant only for N cycles, after which the effect of the previous feature is erased. Thus, two features separated by only N cycles can be detected, as compared to Q cycles in steady-state-based approaches [30]. By monitoring the mismatch signal $e_1 = y - \hat{y}$, or, equivalently, the innovation signal when M is a Kalman filter, the time between features can be reduced, yielding enhanced bandwidth. Thus, in TF-AFM, the tradeoff between resolution and bandwidth is addressed by decoupling the bandwidth from the quality factor Q of the cantilever.

Although the transient term due to a sample feature is not entirely known, certain quantitative characteristics of the transient term in (10) can be derived by analyzing the innovation e_1. Such characteristics can be gleaned from the initial condition response of the linear time-invariant model of the cantilever. Every encounter with the sample, which is modeled as an initial condition reset, results in a transient term, which can be observed as a specific profile in e_1. Thus, e_1 can be matched to such a profile, and the likelihood ratio of a sample encounter versus no-sample encounter can be evaluated in real time. A substantial improvement in resolution of sample features is facilitated by this approach [29].

Experimental Results

A Digital Instruments multimode AFM is used in the experiments. The observer M corresponding to the first mode model of a cantilever ($f_0 = 60.025$ kHz and $Q = 130$) is implemented in an analog circuit. Figure 12(a) shows the amplitude image with sample features superimposed. The sample topography consists of four peaks, which appear at the cantilever separated by 100 μs. It is evident that as soon as the cantilever encounters the first feature near 184.4 ms, the cantilever oscillations decrease, while the effect of the first encounter persists in the deflection signal when the cantilever encounters the second feature at 184.5 ms. However, the signal e_1 dies out within a couple of cycles of the cantilever oscillations [Figure 12(b)] and is near zero before the cantilever encounters the second feature. The innovation, that

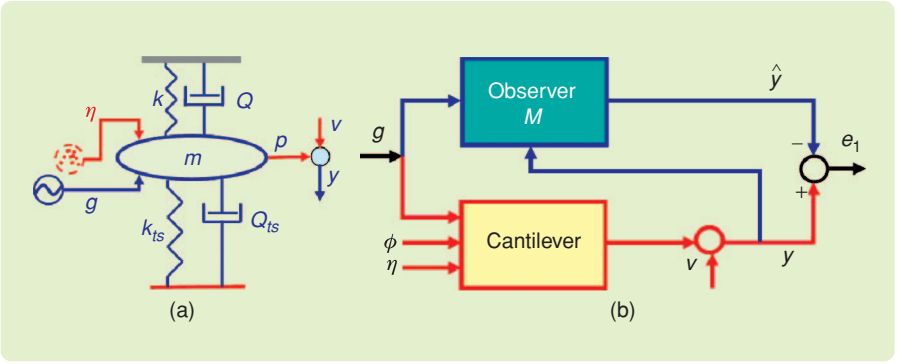

FIGURE 11 (a) A spring-mass-damper schematic of the cantilever-sample interaction and (b) observer architecture for transient force atomic force microscopy. The combined cantilever-sample system model includes the known cantilever parameters k, m, and Q as well as the unknown sample parameters k_{ts} and Q_{ts}. The observer M in (b) is determined from the free cantilever parameters. The output $\hat{y}$ of M and the photodiode output y are compared to produce the innovation signal e_1.

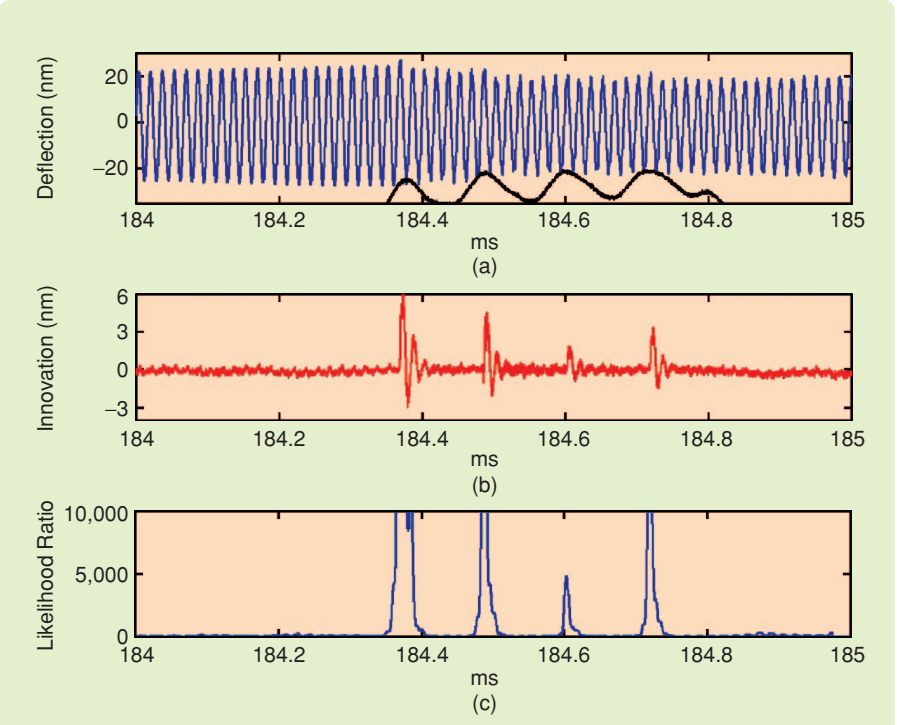

FIGURE 12 (a) Sample topography and deflection signal, (b) innovation signal from transient force atomic force microscopy, and (c) likelihood ratio from transient force atomic force microscopy. In (a) the cantilever deflection signal and sample topography profile (in black) are plotted versus time. The sample topography has four peaks, and the amplitude envelope of the deflection signal is incapable of distinguishing the four peaks. In (b) it is evident that the innovation shows jumps at every peak on the sample topography. In (c) the high contrast in the likelihood ratio obtained as the output of a matched filter yields significant advantages with respect to resolving the peaks in the sample topography.

is, the error signal, resolves the second feature. Note that the cantilever has yet to erase the effects of the first encounter, which is evident from the decreased amplitude of the cantilever oscillations. The model-error-based detection resolves all four features, whereas it is evident that the amplitude envelope of the deflection signal in Figure 12(a) cannot resolve any features after the first one.

Significant enhancement in resolution is possible by correlating the innovation signal with the predetermined profile, which characterizes the effect of surface features modeled as initial-condition resets. This enhancement is evident in the likelihood-ratio plot in Figure 12(c), where the innovation signal is correlated with the profile and the likelihood ratio is evaluated using (10). The zoomed version of the data [Figure 13(b)] shows that the dynamic profile appears in the innovation signal. The large gains in resolution are apparent in the likelihood-ratio plot. These experiments demonstrate the capability of detecting 10,000 b/s using a cantilever with a resonance frequency at 60 kHz. Since the detection rate scales linearly with the cantilever's resonance frequency, a 500-kHz cantilever, available commercially, can reach rates of 1.25×10^5 features per second. Note that TF-AFM, unlike methods that achieve high bandwidth by reducing device dimensions [12], does not impose restrictions on sample size.

Nanopositioning

A typical nanopositioning system used in SPM is comprised of a flexure stage, which provides motion through elastic deformations, piezoelectric actuators that apply forces on the flexure stage, sensors that measure the flexure motion, and a feedback system.

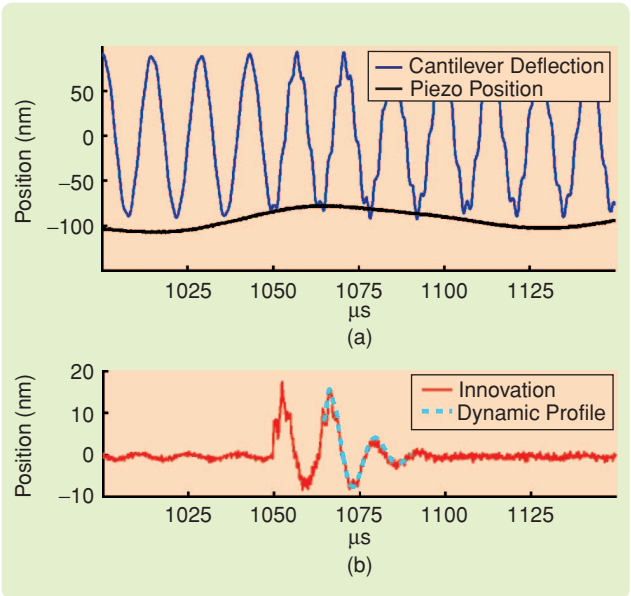

FIGURE 13 (a) Zoomed version of the deflection signal when interacting with a single peak and (b) dynamic profile in transient force atomic force microscopy. In (b) the dynamic profile due to the transient term caused by a sample encounter appears in the innovation signal.

Flexure stages are the preferred hardware for positioning since they provide a large range of motion. Furthermore, flexure stages have no sliding parts, thereby avoiding undesirable effects such as backlash and friction. The flexure stages used in SPM can produce deformations with repeatable atomic-scale resolution with a maximum traversal in the 10–150-μm range.

Piezoelectric material is the preferred choice of actuation primarily because it can facilitate positioning with subnanometer resolution. Piezoelectric actuators can generate large forces that are as high as a few tens of kilonewtons, have fast response times with acceleration rates as high as 10^4 g, are not affected by magnetic fields, and are operable over a wide range of temperatures. Furthermore, piezoelectric actuators require minimal power and low maintenance since they have less wear and tear. In some SPM setups, the piezoelectric actuator comprises the positioning stage, where a flexure stage is not used, although the range of motion is limited. Lateral motion in SPMs is typically sensed by linear variable differential transducers (LVDTs), strain gauges, or optical sensors. State-of-the-art sensors have a resolution of a few angstroms over a bandwidth of 1 kHz.

The performance of a nanopositioning system is characterized by its positioning resolution, tracking bandwidth, and robustness to modeling uncertainties. The resolution of the nanopositioning system is specified in terms of the standard deviation σ of the sensor output when there is no actuation of the positioning stage. The *measurement noise* typically exhibits a zero-mean Gaussian distribution. Thus, 3σ-resolution defined by the measurement noise gives over 99.7% confidence in any signal value that is greater than the resolution. Nanopositioning applications require resolution that ranges from subnanometer to a few hundred nanometers. The tracking bandwidth is the range of reference-signal frequencies that the nanopositioning system can track with a given precision. In closed-loop nanopositioning systems, the range of frequencies over which the magnitude plot of the sensitivity transfer function is below $1/\sqrt{2}$ determines the tracking bandwidth. Typical nanopositioning systems in SPM provide a tracking bandwidth in the range of a few tens of hertz to a few kilohertz. The robustness of the nanopositioning system to modeling uncertainty is characterized in terms of the peak of the magnitude of the sensitivity transfer function; the higher the peak, the less is the robustness. The requirement of robustness is mainly to provide repeatability and, therefore, reliability of experiments.

The main challenges for control design in achieving performance objectives arise from the flexure resonances, the nonlinear effects of the piezoelectric actuation, and the effect of measurement noise on the resolution of the

device. The natural frequencies of mesoscale flexure stages, because of their mass, are typically a few orders lower than the natural frequencies of microscale cantilevers. Therefore, flexure stages become the bottleneck to achieving high scan rates. The phenomenon of piezoelectricity is still poorly understood, and therefore model uncertainty must be addressed in the design of a nanopositioning system.

In many nanopositioning systems that run in open loop, nonlinear piezoelectric effects, such as hysteresis and creep, form the main impediments to attaining high resolution and tracking bandwidth specifications. The most common approach to increasing tracking bandwidth is to increase the resonance frequency of a nanopositioning system by building devices that are sufficiently stiff and small. However, building small scanning devices limits the maximum traversal of the system to a few microns. A feedforward scheme for improving the accuracy of a nanopositioning system is discussed in [31]. Energy-based models of piezoelectric behavior that incorporate the dependence of hysteresis loops on the scan rates are developed and applied to piezoelectric actuators in [32] and [33]. These models, which are based on physical principles, predict a greater number of observed features in experiments than the phenomenological models, such as the Preisach model [31], [34]. Feedforward implementation schemes based on these models thus provide better positioning resolution [32]. The use of charge amplifiers instead of voltage amplifiers is another means for reducing hysteresis [35].

Feedback control design with large gains at low frequencies makes positioning resolution practically independent of piezoelectric nonlinearities, where nonlinear effects become negligible compared to measurement noise. Positioning resolution in a closed-loop nanopositioning system is determined by the complementary sensitivity transfer function, which specifies the bandwidth of the measurement noise that is fed back.

Thus, for closed-loop nanopositioning systems, there is a fundamental tradeoff between the tracking bandwidth and positioning resolution since systems with larger tracking bandwidth allow noise to affect the positioning over a larger frequency range and hence provide poorer positioning resolution. That is, since the sum of sensitivity $S(j\omega)$ and the complementary sensitivity $T(j\omega)$ is unity at all frequencies ω, designing $|S(j\omega)|$ to be small over a large range of frequencies for achieving high tracking bandwidth makes $|T(j\omega)|$ large over these frequencies, which adversely affects the resolution. Furthermore, imposing the rolloff frequency ω_T of $T(j\omega)$ to be near the tracking bandwidth ω_b to avoid large $|T(j\omega)|$ at frequencies beyond ω_b makes the system less robust to modeling uncertainty. This limitation is explained by the Bode integral law, which restricts $\int_0^\infty \log(|S(j\omega)|)d\omega$, and therefore $\int_0^\infty \log(|1-T(j\omega)|)d\omega$, to zero, which implies that the smaller the gap $\omega_T - \omega_b$, the larger the peak in $\log|S(j\omega)|$ in the frequency range (ω_b, ω_T), and, therefore lesser the robustness to modeling uncertainty. In [36]–[38], feedback control design based on robust control theory, primarily $\mathcal{H}_\infty$ control techniques, is used to simultaneously achieve performance objectives on positioning resolution, tracking bandwidth, and robustness to modeling uncertainties. Figures 14 and 15 show experimental results that demonstrate the benefits of an $\mathcal{H}_\infty$ control design with respect to tracking bandwidth, compensation for hysteresis, and repeatability [36].

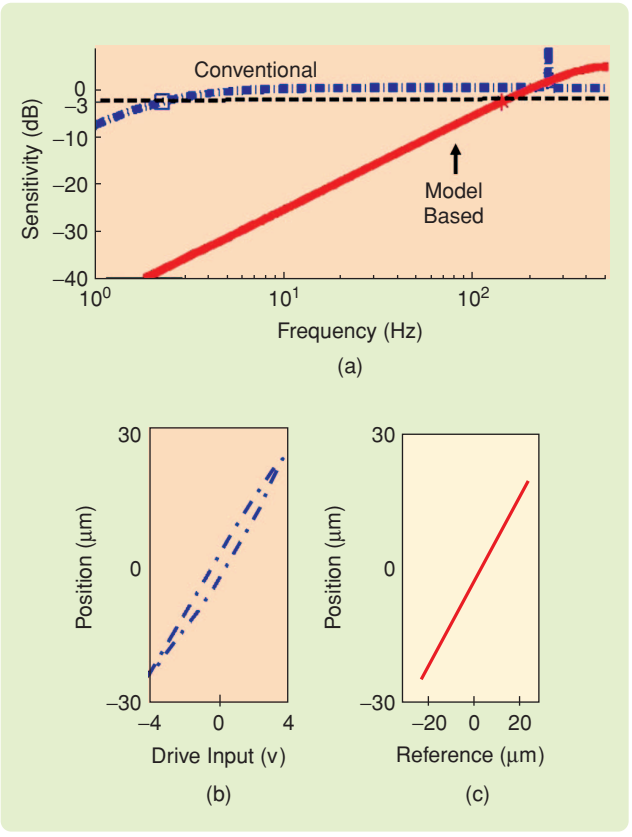

FIGURE 14 (a) Improvement in tracking bandwidth by using an $\mathcal{H}_\infty$ design and (b), (c) the role of $\mathcal{H}_\infty$ design in reducing the effect of hysteresis. The $\mathcal{H}_\infty$ design provides increased tracking bandwidth as is evident from the plot of the magnitude of the sensitivity transfer function versus frequency. The $\mathcal{H}_\infty$ design yields a tracking bandwidth of 138 Hz as opposed to 2.2 Hz from the conventional proportional and double-integral design. The hysteresis curves in (b) are obtained by plotting the sensor output of the nanopositioning system operated in an open-loop manner against the 1-Hz triangular input voltage to the piezoelectric drive. The plot (c) was obtained by giving a 1-Hz triangular input reference signal to the closed-loop nanopositioning system. The hysteresis is quantified in terms of the maximum-input hysteresis and maximum output hysteresis given by the largest width and height, respectively, in the hysteresis loop as a percentage of the input voltage amplitude and the traversal of the positioning system. For a traversal of 45 μm, the maximum-output hysteresis and maximum-input hysteresis are 10% and 7.6%, respectively, in the open loop as opposed to 0.14% and 0.07%, in the closed-loop nanopositioning system.

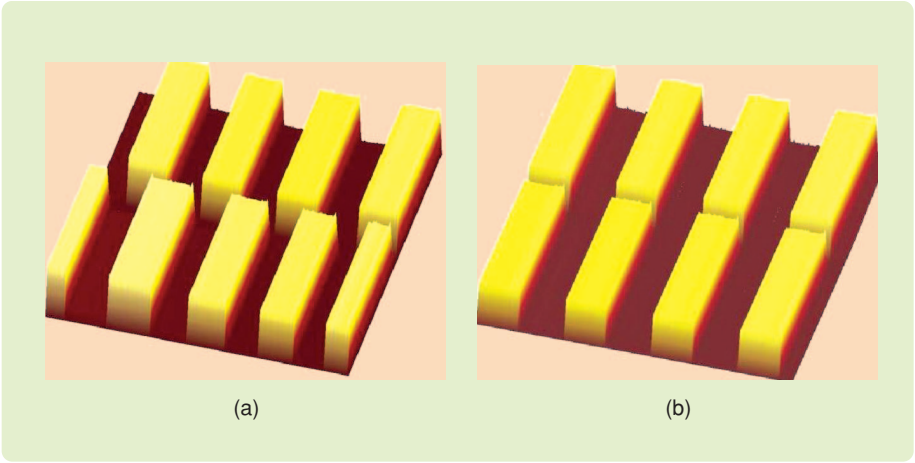

FIGURE 15 (a) Forward and reverse scans of a calibration sample and (b) forward and reverse scans with $\mathcal{H}_\infty$ control. The forward and reverse scan images in the (a) conventional design do not agree with each other and give distorted images of a calibration sample, while the (b) model-based feedback gives high fidelity images in both the forward and reverse scans.

Fundamental limitations on tracking bandwidth and robustness to modeling uncertainties are presented in [38], where a feedback design based on the Glover-McFarlane loop-shaping procedure [39], which wraps a controller around an existing proportional-double-integral controller, achieves over 70% reduction in the peak of the magnitude of the sensitivity transfer function, when compared to the existing design, without compromising the tracking bandwidth. Subnanometer positioning resolution is achieved by a control design presented in [40], which limits the range of frequencies that determine the tracking bandwidth of the positioning system approximately to the frequency content of the reference signal that is known a priori. This design is particularly useful for scanning applications, where high-frequency sinusoidal reference trajectories achieve high scan rates, while high positioning resolution is guaranteed since the range of frequencies where the measurement noise affects the positioning resolution is restricted to a small bandwidth around the reference frequency.

Nanopositioning systems generally have a moving mass for each axis of motion. In contrast to single-mass systems, having a separate mass for each axis avoids the coupling between different axial motions. However, these multi-mass nanopositioning systems are heavier and therefore provide smaller tracking bandwidth than single-mass systems. Multi-input, multi-output control design can be used to decouple the motion in different directions in single-mass nanopositioning systems, thereby achieving larger tracking bandwidths. In [41], a microelectromechanical single-mass nanopositioning system, where each actuator produces motions along multiple axes, is described. Multi-input, multi-output identification and control design methods are used in [41] to decouple different positioning directions, enable tracking of reference trajectories with improved bandwidth, and guarantee acceptable robustness margins.

New Sample Topography Estimate

In most SPM schemes, the control signal, which is applied to the vertical positioner for setpoint regulation, serves as the sample image. The rationale for using the control signal as an estimate of the sample topography is explained by analyzing the schematic model of the AFM in Figure 16(a), where G represents the transfer function from the piezo voltage input u to the piezo displacement. The tip of the cantilever encounters the surface topography as the time signal $d(t) = h(x(t), y(t))$, where $h(\cdot, \cdot)$ represents the sample topography and $(x(t), y(t))$ denotes the lateral coordinates of the tip-sample contact point set by the X-Y scanner. This sample topography signal d is viewed as a disturbance signal that tries to deviate the cantilever deflection signal from its setpoint deflection. Good setpoint regulation over a prespecified bandwidth is achieved by designing K to have large magnitude over the bandwidth. This deduction is made after noting that the transfer function from r to e, which is given by $1/(1 + G(j\omega)K(j\omega))$, is small when $K(j\omega)$ is large. For large values of K, the transfer function from the sample topography d to the control signal u,

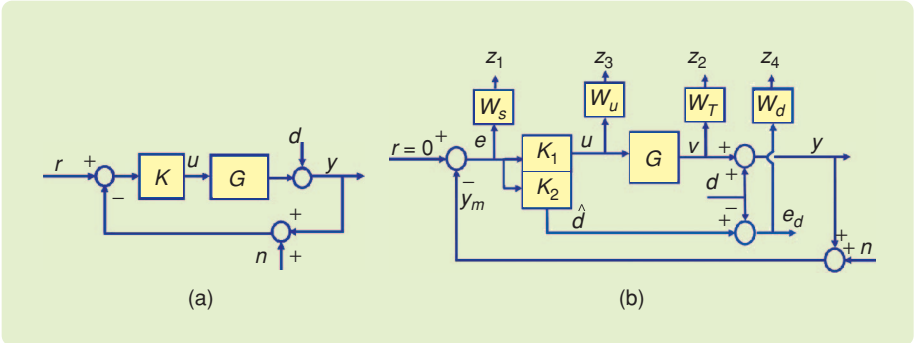

FIGURE 16 (a) A block diagram of the atomic force microscope with sample topography as the disturbance d and (b) block diagram for the model-based scheme for sample-topography estimation. The transfer function G represents the vertical piezoelectric positioner along with the cantilever and photo sensor, where the signals d, r, and n represent the sample topography, setpoint value, and measurement noise. The block $[K_1\ K_2]$ in (b) is designed to achieve simultaneous specifications for setpoint regulation, noise attenuation, and sample-topography estimation.

which is equal to $K(j\omega)/(1 + K(j\omega)G(j\omega))$, can be approximated by $1/G(j\omega)$. Low-bandwidth imaging does not excite the high-frequency dynamics of the positioner. Therefore, the control signal u is a good estimate of the sample topography only when the transfer function $G(j\omega)$ is constant.

However, for high-bandwidth operation, the dynamics of the positioner must be accounted for. The temporal frequency content of d depends on the spatial frequency content of the sample topography as well as the speed at which the sample is scanned. In view of control designs for faster lateral positioning [31], [36], [38], [42], it is necessary to obtain high-bandwidth estimates of d. To achieve good regulation, the control compensates for the positioner dynamics, and thus the control signal is no longer an accurate estimate of the sample topography. Accordingly, a key question to be addressed is whether the positioner dynamics $G(j\omega)$ impose a fundamental limitation on the topography reconstruction in SPMs. The discussion above (see also [43]–[46]) indicates that a compromise must be struck between the bandwidth for sample topography estimation and setpoint regulation. This apparent limitation is resolved by designing two signals, namely, the control signal for setpoint regulation, resolution, and bandwidth, and the sample topography estimate signal for the sample image. In [47], [48] this design is formulated as an optimal control problem.

The resolution of the AFM, which is the smallest topographic change that can be sensed by the AFM system, is largely determined by the noise n introduced by the laser-photodiode measurement system, which limits the minimum topographic change that can be gleaned from the measured signal [Figure 16(a)]. A control system that is badly designed can exacerbate the effect of the measurement noise, thereby reducing the resolution. Key objectives of the feedback control design for vertical positioning other than regulation thus include limiting the effect of the sensor noise n on the piezo movement and restricting the control signal to levels that keep the piezo actuator from saturation.

The schematic of the control design formulation shown in Figure 16(b) encompasses the objectives outlined above. The block $K = [K_1 \;\; K_2]^T$ has two outputs, u and $\hat{d}$. The control signal u is designed for setpoint regulation of the deflection signal y, high-resolution imaging through rolloff of the transfer function from the noise n to the piezo response v, and prevention of the piezo actuator from saturation. The signal $\hat{d}$ is designed to estimate the sample topography d. The design objectives translate to the task of determining a controller that minimizes a performance measure on the weighted regulation error z_1, weighted noise sensitivity z_2, weighted control effort z_3, and weighted topography estimation error z_4. Thus, the external input to the closed-loop system is $w = [r\; n\; d]'$, whereas the variable to be regulated is given by $z = [z_1\; z_2\; z_3\; z_4]'$. We denote the closed-loop map from w to z by $\Phi_{wz}(K)$, where the closed-loop map depends on the controller K. From the discussion above it follows that the relevant control design problem can be cast as

$$\min_{K=[K_1 \;\; K_2] \text{ stabilizing}} \|\Phi_{wz}\|, \tag{11}$$

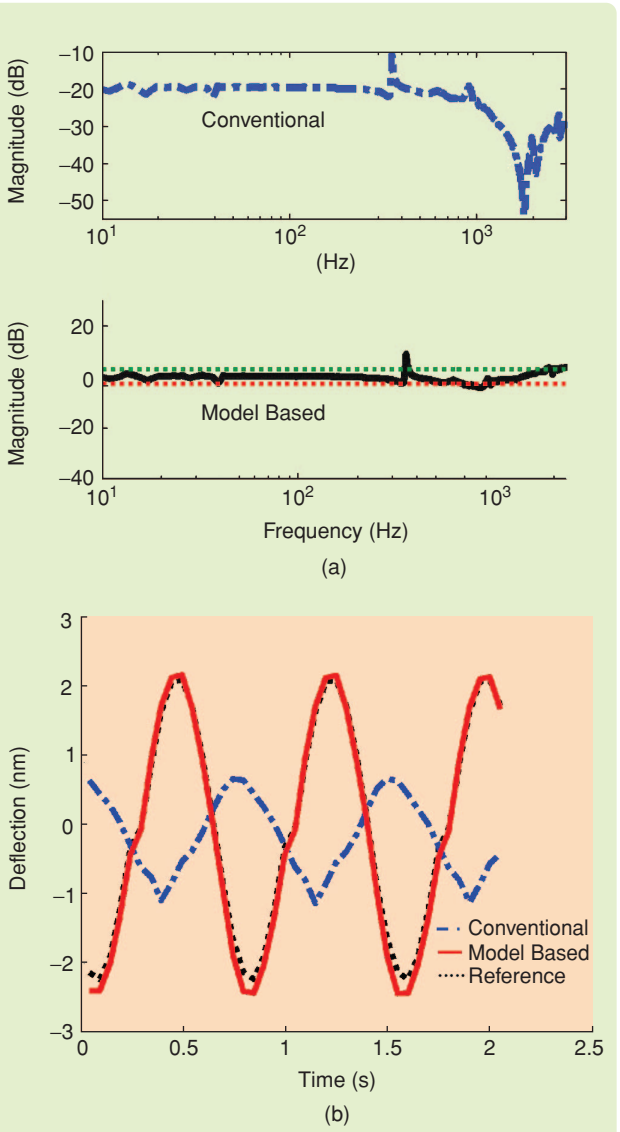

FIGURE 17 (a) Bandwidth improvement of sample-topography estimation with a model-based scheme and (b) comparison of the conventional and model-based scheme for tracking a high-frequency sinusoid. (a) shows the magnitude part of the Bode plot for the closed-loop transfer function from the sample topography d to the conventional estimate signal, the control signal u, and the closed-loop transfer function from the sample topography d to the model-based estimate $\tilde{d}$. It is evident that the conventional transfer function remains roughly constant over the frequency range 0–800 Hz, whereas the model-based transfer function remains within 3 dB over the frequency range 0–3000 Hz. (b) shows that the conventional estimate signal u does not adequately track the 1400-Hz sinusoidal reference signal, whereas, the model-based signal tracks the sample topography with a small error.

where $\|\cdot\|$ is the $\mathcal{H}_\infty$ norm and K is restricted to be stabilizing. A related standard stacked $\mathcal{H}_\infty$ problem is given by

$$\min_{K_1 \text{ stabilizing}} \|\Phi_{w\tilde{z}}\|, \tag{12}$$

where the estimate $\hat{d}$ of the sample topography is not included as an objective and $\tilde{z} = [z_1\ z_2\ z_3]'$.

It can be shown [47], [48] that by solving the standard stacked $\mathcal{H}_\infty$ problem (12), the solution to (11) can be obtained. Indeed, if K_1^o is an optimal solution to (12), then it can be shown that an optimal solution to (11) is given by $K^o = [K_1^o\ K_2^o]$, where K_2^o can be chosen to satisfy $\Phi_{d\hat{d}} = 1$. This result indicates that a precise estimate $\hat{d}$ of the sample topography can be obtained irrespective of the frequency content of the sample topography d. Thus, the objective of setpoint regulation does not compromise the objective of sample topography reconstruction. In contrast to the signal $\hat{d}$, the control signal u, which is traditionally used as the estimate of the sample topography, gives a good estimate of the sample topography only when the topography signal $d(t)$ has low-frequency content. In Figure 17, experimental data is presented that compares the capability of the control effort u and $\hat{d}$ to predict the sample topography. It is evident from the data that u fails to provide a good estimate of the sample topography beyond 800 Hz, whereas $\hat{d}$ provides a good estimate up to 3000 Hz.

We note that perfect sample topography reconstruction is possible in the absence of noise and in the absence of uncertainty in the AFM model used to determine the controller by solving (11). In [48] it is shown that the tradeoff between the robustness of this design to modeling uncertainties and the accuracy of image reconstruction can be managed by appropriate design of the weights attributed to the various objectives.

CONCLUSIONS

This article describes new perspectives on SPM-related science and technology, based on systems and control theory. These perspectives have led to a better understanding of SPM technology, overcome hurdles that limited the efficacy of SPM, and resulted in new modes of SPM-based interrogation. ThNcAFM, based on systems principles, has made it possible to image with resolution as high as 0.25 Å in ambient conditions. The orders-of-magnitude improvements achieved in areas such as precision positioning, sample imaging, and sample detection rates emphasize the potential of systems tools in nanotechnology.

The concept of using models in online operation has significant potential for SPM. For instance, TF-AFM, which uses models for online operation, resolves competing objectives of high resolution and detection rate by using a design from a systems perspective that makes detection bandwidth independent of the quality factor of the probe and, therefore, independent of resolution. The systems perspective also facilitates the interpretation of data since it provides a precise means for delineating the effects of the inherent dynamics of the interrogation system from the properties of the sample being probed.

Devices such as SPMs are sensitive to operating conditions, ambient conditions, and modeling inaccuracies. Modern control theory provides a framework where such challenges can be effectively addressed. This aspect translates to reliable experiments in terms of repeatability, which is crucial in many nanoscience studies.

ACKNOWLEDGMENT

This research was partially supported by NSF under the grants ECS 0449310 CAR, ECS-0601571, ECS-0330224, CMS-0201516, and ECS-9733802. We wish to thank Kishan Baheti for facilitating workshops and sessions in scanning probe microscopy, which have led to fruitful collaborations among researchers from industry and academia.

DEDICATION

The authors dedicate this article to their parents, Smt. S. Subhadra and Shri S. Prasada Rao.

REFERENCES

[1] R. Feynman, "There's plenty of room at the bottom—an invitation to enter a new field of physics," *Eng. Science*, vol. 23, pp. 22–36, 1960.
[2] G. Binnig, H. Rohrer, Ch. Gerber, and E. Weibel, "Tunnelling through a controllable vacuum gap," *Appl. Phys. Lett.*, vol. 40, no. 2, pp. 178–180, 1982.
[3] G. Binnig, H. Rohrer, Ch. Gerber, and E. Weibel, "Surface studies by scanning tunneling microscopy," *Phys. Rev. Lett.*, vol. 49, no. 1, pp. 57–61, 1982.
[4] G. Binnig, H. Rohrer, Ch. Gerber, and E. Weibel, "7 × 7 reconstruction on si(111) resolved in real space," *Phys. Rev. Lett.*, vol. 50, no. 2, pp. 120–123, 1983.
[5] National Science and Technology Council, Committee on Technology, Subcommittee on Nanoscale Science, Engineering and Technology, "National nanotechnology initiative: The initiative and its implementation plan," July 2000. [Online]. Available: http://www.nano.gov/nni2.pdf
[6] D. Sarid, *Scanning Force Microscopy with applications to Electric, Magnetic and Atomic Forces*. London, U.K.: Oxford Univ. Press, 1991.
[7] M.V. Salapaka, H.S. Bergh, J. Lai, A. Majumdar, and E. McFarland, "Multi-mode noise analysis of cantilevers for scanning probe microscopy," *J. Appl. Phys.*, vol. 81, no. 6, pp. 2480–2487, Mar. 1997.
[8] J.N. Israelachvili, *Intermolecular and Surface Forces*. New York: Academic, 1985.
[9] F.J. Giessibl, *Noncontact Atomic Force Microscopy*. New York: Springer-Verlag, 2002.
[10] T. Eguchi and Y. Hasegawa, "High resolution atomic force microscopic imaging of the si(111)-7×7 surface: Contribution of short-range forces to the images," *Phys. Rev. Lett.*, vol. 89, no. 26, p. 266105, 2002.
[11] F.J. Giessibl, S. Hembacher, H. Bielefeldt, and J. Mannhart, "Subatomic features on the silicon (111)-(7×7) surface observed by atomic force microscopy," *Science*, vol. 289, pp. 422–425, July 2000.
[12] T. Ando, N. Kodera, E. Takai, D. Maruyama, K. Saito, and A. Toda, "A high-speed atomic force microscope for studying biological macromolecules," *Proc. Nat. Acad. Sci.*, vol. 98, no. 22, p. 034106, 2001.
[13] A. Sebastian, M.V. Salapaka, D. Chen, and J.P. Cleveland, "Harmonic balance based analysis for tapping-mode AFM," in *Proc. American Control Conf.*, San Diego, 1999, pp. 232–236.
[14] A. Sebastian, M.V. Salapaka, D. Chen, and J.P. Cleveland, "Harmonic and power balance tools for tapping-mode atomic force microscope," *J. Appl. Phys.*, vol. 89, no. 11, pp. 6473–6480, June 2001.
[15] A. Sebastian and M.V. Salapaka, Analysis of Periodic Solutions in Tapping Mode AFM. *Mathematical Theory of Networks and Systems*, University of Notre Dame, South Bend, Aug. 12, 2002 [Online]. Available: http://www.nd.edu/mtns/papers/5815.pdf

[16] A. Sebastian and M.V. Salapaka, "Amplitude phase dynamics and fixed points in tapping-mode atomic force microscopy," in *Proc. American Control Conf.*, Boston, June 2004, pp. 2499–2504.
[17] S. Salapaka, M. Dahleh, and I. Mezic, "On the dynamics of a harmonic oscillator undergoing impacts with a vibrating platform," *Nonlinear Dynam.*, vol. 24, pp. 333–358, 2001.
[18] S. Hu and A. Raman, "Chaos in atomic force microscopy," *Phys. Rev. Lett.*, vol. 036107, pp. 1–3, Jan. 2006.
[19] A.E. Pelling, S. Sehati, E.B. Gralla, J.S. Valentine, and J.K. Gimzewski, "Local nanomechanical motion of the cell wall of Saccharomyces cerevisiae," *Science*, vol. 305, no. 5687, pp. 1147–1150, 2004.
[20] V.F. Pisarenko, "The retrieval of harmonics from a covariance function," *Geophys. J. R. Astron. Soc.*, vol. 33, pp. 347–366, 1973.
[21] H. Holscher, U.D. Schwarz, and R. Wisendanger, "Calculation of frequency shift in dynamic force microscopy," *Appl. Surf. Sci.*, vol. 140, pp. 344–351, 1999.
[22] R. Erlandsson and L. Olsson, "Force interaction in low amplitude ac-mode atomic force microscopy: Cantilever simulations and comparison with data from si(111)7 × 7," *Appl. Phys. A: Mat. Sci. Process.*, vol. 66, pp. S879–S883, 1998.
[23] A. Oral, R.A. Grimble, H.O. Ozer, P.M. Hoffmann, and J.B. Pethica, "Quantitative atom resolved force gradient imaging using noncontact atomic force microscopy," *Appl. Phys. Lett.*, vol. 79, no. 12, pp. 1915–1917, 2001.
[24] P.M. Hoffmann, S. Jeffery, J.B. Pethica, H.Ö. Özer, and A. Oral, "Energy dissipation in AFM and atomic loss processes," *Phys. Revi. Lett.*, vol. 87, p. 265502, 2001.
[25] P.M. Hoffmann, S. Jeffery, A. Oral, R.A. Grimble, H.O. Ozer, and J.B. Pethica, "Nanomechanics using an ultra-small amplitude AFM," in *Mater. Res. Soc. Symp. Proc.*, vol. 649, pp. Q9.2.1–6, 2001.
[26] S.P. Jarvis, H. Yamada, S.I. Yamamoto, H. Tokumoto, and J.B. Pethica, "Direct mechanical measurement of interatomic potential," *Nature*, vol. 384, pp. 247–249, 1996.
[27] S.P. Jarvis, M.A. Lantz, U. Durig, and H. Tokumoto, "Off resonance ac mode force spectroscopy and imaging with an atomic force microscope," *Appl. Surf. Sci.*, vol. 140, pp. 309–313, 1999.
[28] D.R. Sahoo, A. Sebastian, and M.V. Salapaka, "Transient-signal-based sample-detection in atomic force microscopy," *Appl. Phys. Lett.*, vol. 83, no. 26, p. 5521, Dec. 2003.
[29] D.R. Sahoo, A. Sebastian, and M.V. Salapaka, "Harnessing the transient signals in atomic force microscopy," *Int. J. Robust Nonlinear Control*, vol. 15, pp. 805–820, 2005.
[30] R. Wisendanger, *Scanning Probe Microscopy and Spectroscopy*. Cambridge, MA: Cambridge Univ. Press, 1994.
[31] D. Croft, G. Shedd, and S. Devasia, "Creep, hysteresis and vibration compensation for piezoactuators: Atomic force microscopy application," *J. Dynam. Syst., Measure. Control*, vol. 123, pp. 35–43, 2001.
[32] A.G. Hatch, R.C. Smith, T. De, and M.V. Salapaka, "Construction and experimental implementation of a model-based inverse filter to attenuate hysteresis in ferroelectric transducers," *IEEE Trans. Contr. Syst. Technol.*, vol. 14, no. 6, pp. 1058–1069, 2006.
[33] R.C. Smith, A.G. Hatch, T. De, M.V. Salapaka, R.C.H. del Rosario, and J.K. Raye, "Model development for atomic force microscope stage mechanisms," *SIAM J. Appl. Math.*, vol. 66, no. 6, pp. 1998–2026, 2006.
[34] P. Ge and M. Jouaneh, "Tracking control of a piezoceramic acuator," *IEEE Trans Contr. Syst. Technol.*, vol. 4, no. 3, pp. 209–216, May 1996.
[35] B. Bhikkaji, M. Ratnam, A.J. Fleming, and S.O.R. Moheimani, "High-performance control of piezoelectric tube scanners," *IEEE Trans. Contr. Syst. Technol.*, vol. 5, no. 5, pp. 853–866, Sept. 2007.
[36] S. Salapaka, A. Sebastian, J.P. Cleveland, and M.V. Salapaka, "High bandwidth nano-positioner: A robust control approach," *Rev. Sci. Instrum.*, vol. 73, pp. 3232–3241, 2002.
[37] G. Schitter, P. Menold, H.F. Knapp, F. Allgower, and A. Stemmer, "High performance feedback for fast scanning atomic force microscopy," in *Proc. American Control Conf.*, Denver, 2003, pp. 3720–3725.
[38] A. Sebastian and S. Salapaka, "Design methodologies for robust nano-positioning," *IEEE Trans. Contr. Syst. Technol.*, vol. 13, no. 6, pp. 868–876, 2005.
[39] D. McFarlane and K. Glover, "A loop shaping design procedure using $\mathcal{H}_\infty$ synthesis," *IEEE Trans. Automat. Contr.*, vol. 37, no. 6, pp. 759–769, June 1992.
[40] A. Shegaonkar and S. Salapaka, "Making high resolution positioning independent of scan rates: A feedback approach," *Appli. Phys. Lett.*, vol. 91, p. 203513, 2007.
[41] J. Dong, S. Salapaka, and P. Ferreira, "Robust MIMO control of a parallel kinematics nano-positioner for high resolution high bandwidth tracking and repetitive tasks," in *Proc. Control Decision Conf.*, New Orleans, LA, Dec. 2007, pp. 4495-4500.
[42] A. Daniele, S. Salapaka, M.V. Salapaka, and M. Dahleh, "Piezoelectric scanners for atomic force microscopes: design of lateral sensors, identification and control," in *Proc. American Control Conf.*, San Diego, 1999, pp. 253–257.
[43] K.E. Rifai, O.E. Rifai, and K. Youcef-Toumi, "On dual actuation in atomic force microscopes," in *Proc. American Control Conf.*, Boston, MA, 2004, pp. 3128–3133.
[44] G. Schitter, P. Menold, H.F. Knapp, F. Allgower, and A. Stemmer, "High performance feedback for fast scanning atomic force microscopes," *Rev. Sci. Instrum.*, vol. 72, no. 8, pp. 3320–3327, Aug. 2001.
[45] G. Schitter, F. Allgower, and A. Stemmer, "A new control strategy for high speed atomic force microscopy," *Nanotechnology*, vol. 15, no. 1, pp. 108–114, 2004.
[46] A. Sebastian, J.P. Cleveland, and M.V. Salapaka, "Robust control approach to atomic force microscopy," in *Proc. IEEE Conf. Decision Control*, Maui, HI, 2003, pp. 3443–3444.
[47] S. Salapaka, T. De, and A. Sebastian, "Sample-profile estimate for fast atomic force microscopy," *Appl. Phys. Lett.*, vol. 87, p. 053112, 2005.
[48] S. Salapaka, T. De, and A. Sebastian, "A robust control based solution to the sample-profile estimation problem in fast atomic force microscopy," *Int. J. Robust Nonlinear Contr.*, vol. 15, pp. 821–837, 2005.
[49] P. Vettiger, G. Cross, M. Despont, U. Drechsler, U. Durig, B. Gotsmann, W. Haberele, M.A. Lantz, H. Rothuizen, R. Stutz, and G. Binnig, "The millipede-nanotechnology entering data storage," *IEEE Trans. Nanotechnol.*, vol. 1, no. 1, pp. 39–55, 2002.
[50] J. Xu, M. Lynch, J.L. Huff, C. Mosher, S. Vengasandra, G. Ding, and E. Henderson, "Microfabricated quill-type surface patterning tools for the creation of biological micro/nano arrays," *IEEE Trans. Nanotechnol.*, vol. 6, no. 2, pp. 1387–2176, 2004.

AUTHOR INFORMATION

Srinivasa M. Salapaka (salapaka@uiuc.edu) received the B.Tech. degree in mechanical engineering from the Indian Institute of Technology, Madras, in 1995 and the M.S. and Ph.D. degrees in mechanical engineering from the University of California at Santa Barbara in 1997 and 2002, respectively. During 2002–2004, he was a postdoctoral associate in the Laboratory for Information and Decision Systems, Massachusetts Institute of Technology, Cambridge. Since 2004, he has been a faculty member in the Mechanical Engineering Department at the University of Illinois, Urbana-Champaign. His research interests are nanotechnology, combinatorial resource allocation, and numerical analysis of integral equations. He is a 2005 CAREER award recipient. He can be contacted at the Mechanical Engineering Department, University of Illinois, Urbana-Champaign, 362C Mechanical Engineering Building, 1206 W. Green Street, Urbana, IL 61801 USA.

Murti V. Salapaka received the B.Tech. degree in mechanical engineering from Indian Institute of Technology, Madras, in 1991 and the M.S. and Ph.D. degrees in mechanical engineering from the University of California at Santa Barbara, in 1993 and 1997, respectively. He was a faculty member in the Electrical and Computer Engineering Department at Iowa State University from 1997 to 2007. Currently, he is a faculty member in the Electrical and Computer Engineering Department at the University of Minnesota, Minneapolis. His research interests are nanotechnology, multiple-objective robust control, and distributed and structural control. He is a 1997 National Science Foundation CAREER award recipient.